Computation of Prop-Fan Engine Installation Aerodynamics

C.W. Boppe* and B.S. Rosen†
Grumman Corporation, Bethpage, New York

A computational method has been enhanced to permit numerical evaluations of transonic aerodynamic phenomena associated with prop-fan engine installations. Comparisons with experimental data and results using other algorithms provide a basis to determine which aspects of the physical flow and the computerized flow simulation are most important. Features of the prop-fan slipstream and engine nacelle are modeled. In addition, a wind tunnel test was conducted to study interference effects generated by a simple nacelle embedded in a wing surface. Observations related to future engineering applications are included.

Nomenclature

c = chord length
C_D = drag coefficient
C_L = lift coefficient
C_M = moment coefficient
C_p = pressure coefficient
c_l = section lift coefficient
F = nacelle shape function
M = Mach number
p = pressure
q = dynamic pressure
r = radial distance
R = slipstream radius
W = slipstream swirl angle
$\mathfrak{L}$ = centerline
α = angle of attack
γ = specific heat ratio
Δ = mesh spacing, increment
ξ,η = skewed coordinate system
η = wing span position
φ = perturbation velocity potential

Subscripts

i,j = grid indices
MAC = mean aerodynamic chord
T = total
x,y,z = partial derivatives
∞ = freestream

Introduction

HIGH-speed ($M=0.7$, 0.8) propellers called prop-fans provide a means for attaining propulsive efficiency levels that are higher than those for current technology turbofans. To ensure that the integrated prop-fan concept will truly advance total aircraft efficiency, propulsor-airframe interference effects must be minimized. Many engine installation schemes have been proposed, including pusher, tractor, and counter-rotating designs. The tractor scheme is appropriate for initial computational investigations as it incorporates all of the geometric and aerodynamic aspects of the expected integration problem and, in a sense, represents the most difficult case for design. Since historical design efforts do not exist and experimental data bases are somewhat limited, the potential contributions that can be made by today's computational methods are high.

To date, one of the most extensive computational treatments of prop-fan integration has been accomplished using "panel" methods.[1] This type of potential flow approach provides flexibility to treat anticipated complex geometric arrangements and an attempt was made to predict the drag increments required to assess performance characteristics. One aspect of this approach that deserves further study is the ability to predict detailed chordwise pressure distributions which will exhibit shock wave discontinuities at prop-fan transonic cruise conditions. This would enhance the ability to predict wave drag losses and flow separation.

A number of nonlinear, compressible flow, relaxation schemes[2-6] have been developed to treat this problem. Formulations for the classical transonic small perturbation equation, full potential equation, and Euler's equations have been described. These studies provide good qualitative agreement with available experimental data, but details of pressure fields are not resolved. In some cases, flow separation impairs comparisons. Lack of pressure field detail may, in part, explain the traditional failure of computational methods to predict absolute and most incremental drag effects which are needed during design for performance estimates. The designer is obliged to use predicted shock wave strengths, locations, and wing spanwise loading to piece together wave, lift-induced, and friction drag components.

A numerical/experimental study was conducted to assess the ability of a relatively high grid density computational method[7] to predict pressure details and incremental drag levels. This scheme features an extended transonic small-perturbation equation coupled with mesh-system embedding and simple planar boundary conditions which provide modeling flexibility comparable to that of panel methods. Perhaps most importantly, a high-density grid (100 points chordwise) is implemented to resolve flow details.

Problem Description

Prop-fan engine installations present a design problem to the configuration aerodynamicist that is quite different than that of turbofan engine installations. Fundamentally, it can be expected that propulsion/airframe interaction phenomena will be considerably stronger for prop-fan arrangements primarily due to anticipated proximity of airframe, propulsor components, and high-energy stream regions.

An engine nacelle which is embedded in the wing surface is the most common installation now proposed. At high speeds, the embedded nacelle is expected to alter the wing shock wave pattern and span-load, and it might also induce flow separation. This arrangement has been sketched in Fig. 1. Wave, lift-

Received March 14, 1985; revision received Dec. 30, 1985.

*Technical Specialist in Aerodynamics. Member AIAA.
†Senior Engineer in Aerodynamics.

induced, and viscous drag components will increase unless these adverse interference effects are compensated for in the design process.

Designers seeking computational tools to augment the installation integration effort must decide which components of the problem should be modeled or represented in the flow simulation. This is important because modeling the complete physical flow with all its attributes is not possible with current computational technology levels. Approximations must be made. A suggested ranking of importance for different problem components of a typical tractor application is 1) basic wing flow simulation, 2) nacelle contour interference, 3) slipstream swirl, 4) slipstream q and P_T increments, 5) engine inlet and exhaust flows, and 6) viscous dissipation and redistribution of slipstream flow.

This ranking is based on past experimental and computational studies.[2-6] The scheme to be presented will address the first four items only. Key elements must be treated and validated to computationally predict drag increments or provide sufficient flow details (shock position/strength, spanload, and separation prediction) to permit drag estimates to be composed external to the computational method.

Basic Algorithm Description

Computational studies are performed using an extended transonic small-perturbation code.[7] Boundary conditions are imposed in the wing plane and the wake is represented by a double-valued plane of points across which a jump in velocity potential is enforced. The flow equation contains extra cross-flow terms (when compared to the classical transonic small-perturbation equation) which make it possible to resolve shock waves with appreciable sweep:

$$[1-M_\infty^2-(\gamma+1)M_\infty^2\varphi_x-\frac{\gamma+1}{2}M_\infty^2\varphi_x^2]\varphi_{xx}-2M_\infty^2\varphi_y\varphi_{xy}$$
$$+[1-(\gamma-1)M_\infty^2\varphi_x]\varphi_{yy}+\varphi_{zz}=0 \qquad (1)$$

Pressure coefficients on wing surfaces are computed using the following equation:

$$C_p=-[2\varphi_x+(1-M_\infty^2)\varphi_x^2+\varphi_y^2] \qquad (2)$$

In terms of flow equation and boundary condition complexity, the present formulation is somewhat more complicated than the small-perturbation formulation[2] but simpler than full potential and Euler formulations.[3-6] A high-density grid system embedded along the wing span provides 100 evenly spaced grid points between wing chord leading and trailing edges. Spanwise grid lines "cut" the wing at intervals which average between 5% and 7% of wing half-span. Treatment of wing viscous effects is described in Ref. 7. Nonconservative differencing is used throughout.

Clean Wing Flow Simulations

A number of investigators[2,3,5] have suggested that small-perturbation formulations are inadequate for treating blunt, thick, supercritical airfoil sections that might be used for high-speed prop-fan configuration wing designs. High gradients induced by the propeller slipstream could also result in velocity disturbances which violate small-perturbation assumptions. If this is the case, a full potential equation formulation might be required. In addition, modeling of slipstream rotational effects could be important and this would suggest a scheme based on Euler's equations. Since computations were eventually to be performed for complex wing-body-nacelle-slipstream arrangements, a study was conducted to identify whether or not there were fundamental limitations inherent in small-perturbation approximations which would compromise even clean wing flow predictions.

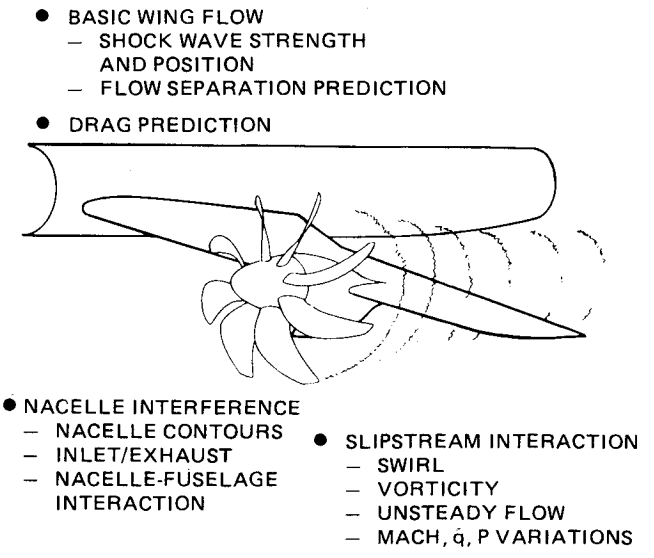

Fig. 1 Flow simulation considerations for prop-fan engine installation applications.

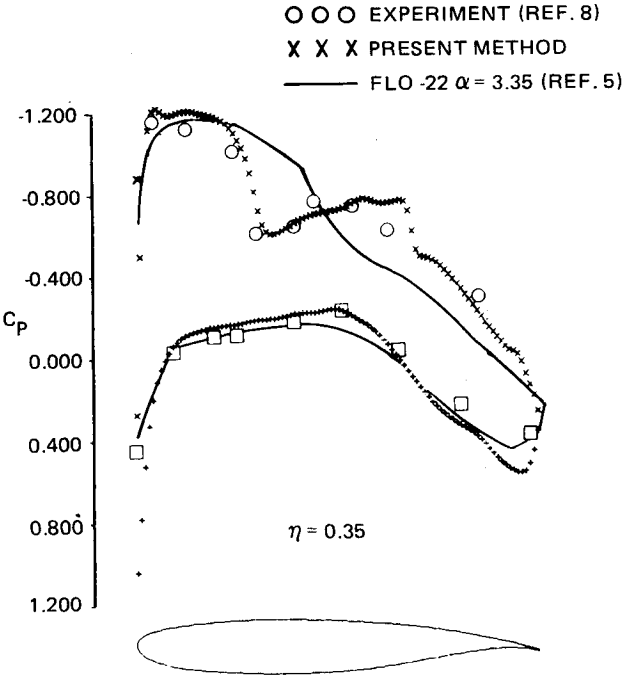

Fig. 2 Wing pressure distribution correlation, $M=0.80$, $\alpha=3$ deg.

Experimental data provided by Welge and Crowder[8] is useful for evaluating slipstream models. The thick, blunt, supercritical wing shape tested can also be studied to identify any limitations of a small-perturbation approach. Wing-body configuration data for $M=0.80$, $\alpha=3$ deg are compared to computational predictions in Fig. 2. Full potential code (FLO-22) results[5] are also included. FLO-22 results do not permit an exact comparison because body surface and wing viscous effects are not modeled, but an interesting observation can still be made. The high grid density small-perturbation scheme appears to predict details of the wing double shock wave system better than the full potential code.

A similar correlation set was generated for a flow condition of $M=0.80$, $\alpha=1.83$ deg. Computed results[6] obtained with a full potential equation, finite volume formulation (FLO-28) can be superimposed for comparison purposes. Fig. 3 shows experiment/analysis agreement for this case, which also exhibits an interesting double shock wave system.

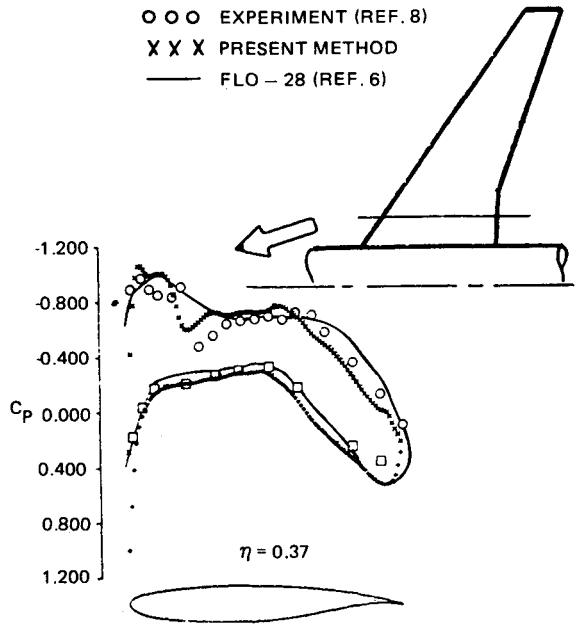

Fig. 3 Wing pressure distribution correlation, $M=0.80$, $\alpha=1.83$ deg.

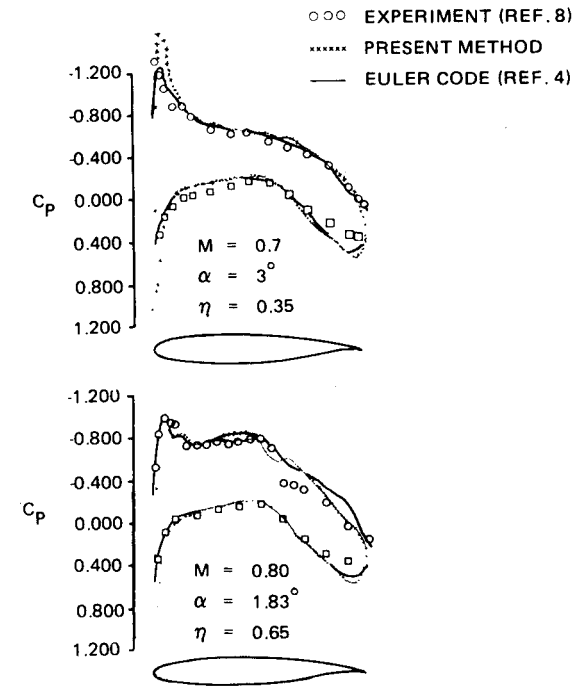

Fig. 4 Wing pressure distribution correlation.

Finite volume code predictions do not show good shock wave resolution. This is particularly noticeable at the forward shock location. It is assumed that this resolution problem is related to a smearing effect inherent in the finite volume formulation. The FLO-28 simulation includes the body shape, but apparently no boundary layer was added. This will affect FLO-28 predicted aft-end load levels, but no significant impact on shock wave resolution is anticipated.

Euler code results[4] were used to construct Fig. 4, which includes comparisons at one wing station for $M=0.70$, $\alpha=3$ deg flow and one station for $M=0.80$, $\alpha=1.83$ deg flow. In this case, the Euler method was coupled with a scheme to predict wing boundary layer effects. It can be seen that small-perturbation results show slightly better agreement at high-speed conditions, while Euler results are slightly better at low-speed conditions.

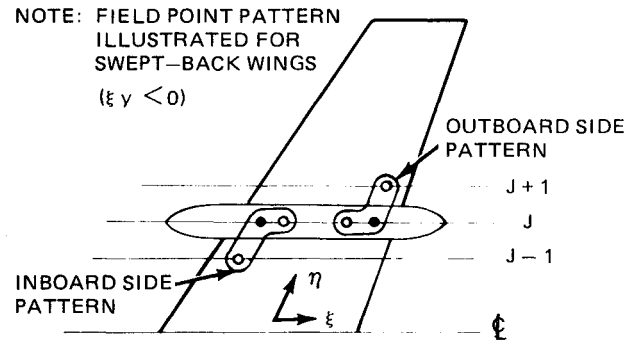

Fig. 5 Grid points used to compute embedded nacelle inboard/outboard boundary conditions.

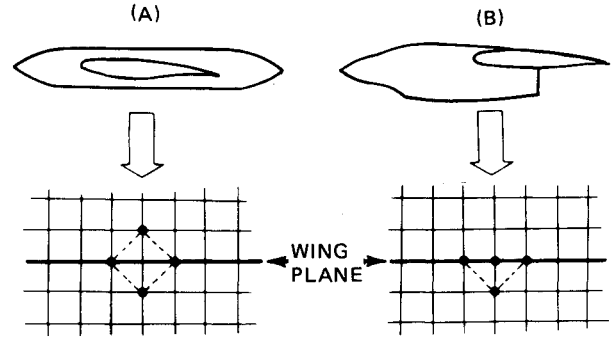

Fig. 6 Nacelle grid point patterns for central and low mount positions.

These analysis/experiment/analysis comparisons indicate that there is no significant penalty associated with implementation of small-perturbation schemes for treating wings with blunt, thick, supercritical sections. In fact, the present formulation has demonstrated an ability to resolve flow details better than more sophisticated codes. It is conceivable, then, that grid resolution and finite-difference approximations can, at times, play a more important role in determining flow simulation quality than terms included in the governing flow equation. With this foundation established, an effort was initiated to predict nacelle and slipstream interference effects.

Nacelle Interference Effects

Modeling of nacelle surfaces which are embedded in a wing has been accomplished by splitting the wing grid relaxation process into two segments. One represents the region between the fuselage side and the inboard nacelle side. Another region starts at the outboard nacelle side and ends at the wrong tip. Special boundary conditions are required to simulate the nacelle side in both regions. Dummy flowfield potentials are computed and positioned inside the nacelle; this has been sketched in Fig. 5.

Special first-order accurate difference operators are employed to ensure a stable relaxation process. Dummy potential values computed for the nacelle outboard side are generated using the following expression:

$$\varphi_{i,j}=\left[\frac{\eta_y}{\Delta\eta}\varphi_{i,j+1}-\frac{\xi_y}{\Delta\xi}\varphi_{i-1,j}-F_x\right]\Big/\left(\frac{\eta_y}{\Delta\eta}-\frac{\xi_y}{\Delta\xi}\right) \quad (3)$$

A similar equation is used to complete dummy potential values required to solve for the inboard nacelle side:

$$\varphi_{i,j}=\left[\frac{\eta_y}{\Delta\eta}\varphi_{i,j-1}-\frac{\xi_y}{\Delta\xi}\varphi_{i+1,j}+F_x\right]\Big/\left(\frac{\eta_y}{\Delta\eta}-\frac{\xi_y}{\Delta\xi}\right) \quad (4)$$

Both expressions are obtained by substituting appropriate difference approximations (see Fig. 5) in the following equation:

$$\varphi_y = \varphi_\xi \xi_y + \varphi_\eta \eta_y = F_x \tag{5}$$

This scheme is suitable for simulating a nacelle in the wing embedded fine grid system. Additional provisions must be made for representing a nacelle in the global crude grid system. Nacelle boundary potential values are computed using the surface flow tangency condition and velocities extrapolated inward from surrounding grid points. These values are fixed during a relaxation sweep. Numerical experiments suggested that grid point patterns illustrated in Fig. 6 would be satisfactory. The diamond model is suitable for nacelles which are centrally mounted on the wing. The half-diamond works well for nacelles which are mounted low. By implementing appropriate tangency boundary conditions, nacelles of arbitrary contour can be simulated with this scheme. For cases included herein, only axisymmetric surfaces are modeled.

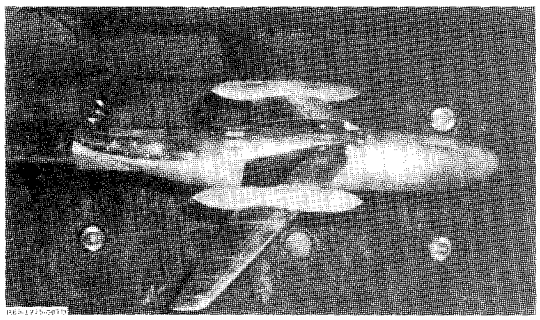

Fig. 7 Model with nacelles embedded in wing surface in NASA Langley Research Center 16-ft transonic wind tunnel.

To validate the simple axisymmetric nacelle model, a cooperative effort was initiated with the Propulsion Branch at NASA's Langley Research Center. A test configuration was specifically set up to be as simple as possible for analysis using the computational method. Large nacelle shapes representing a prop-fan pusher or tractor arrangement were mounted at the planform break on a supercritical wing transport configuration designated USB. Pods were centrally mounted above and below the wing; side contours were straight; and pod-wing junctures (left and right) were positioned at existing pressure tap rows. This configuration is shown in Fig. 7.

Correlations with experimental data for this special model can be found in Fig. 8. Nacelle on/off effects can be identified. Note that nacelle-off comparisons were performed at $M=0.80$, while nacelle-on comparisons were performed at $M=0.75$. The lower nacelle-on Mach number was selected because of significant nacelle induced flow separation at the higher Mach number. Lack of fairings in the wing-nacelle juncture region might cause this. Overall agreement is good but some discrepancies can be identified near the inboard juncture leading edge. This might be attributed to the

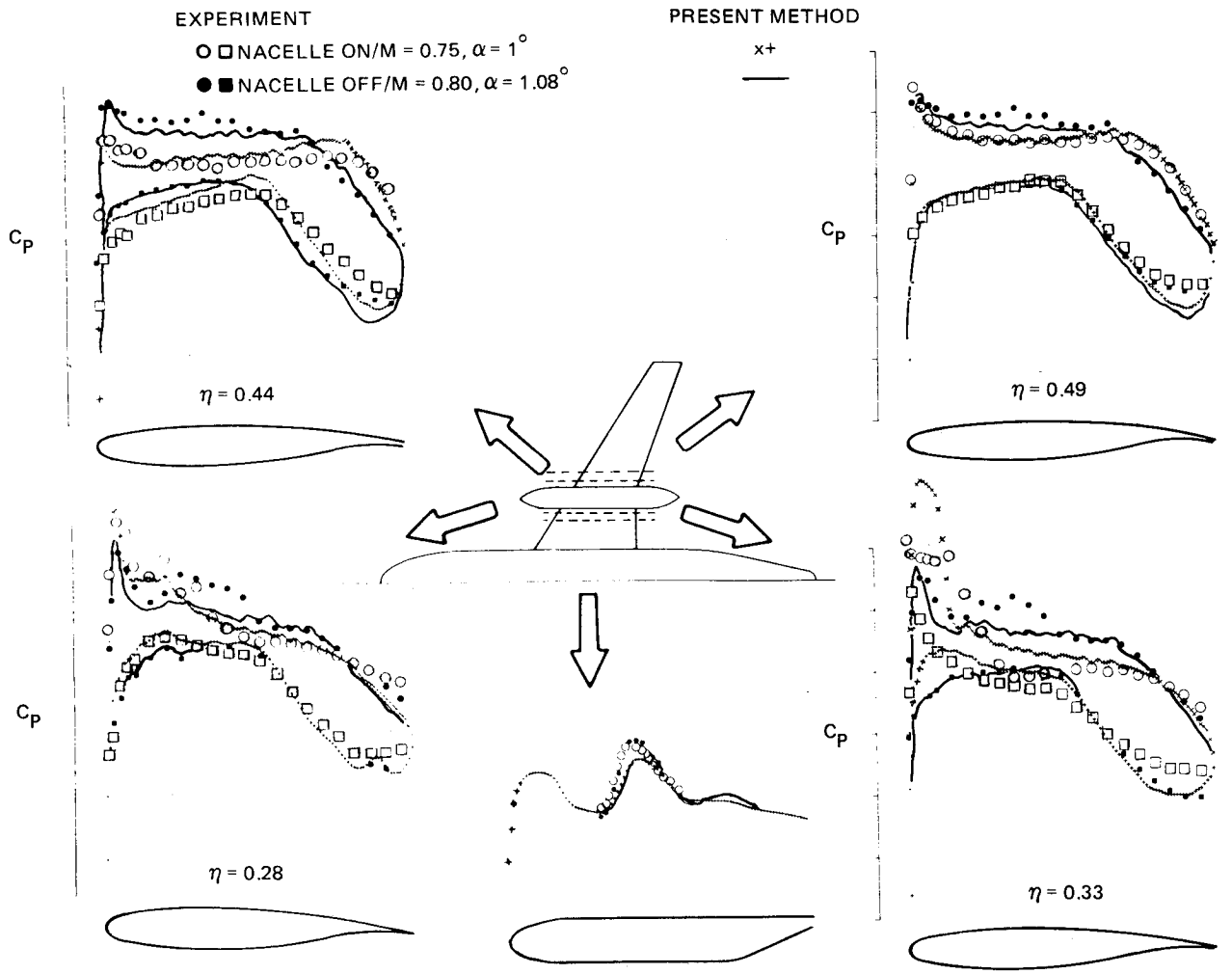

Fig. 8 Wing and fuselage pressure distribution for effect of wing-mounted nacelle.

relatively coarse representation of the nacelle surface in the global crude grid system (32 grid points) and, of course, the possibility of flow separation at the inboard juncture leading edge still exists.

Table 1 provides a comparison of the predicted and experimental lift, drag, and moment increments generated by the nacelles. Poor agreement might be the result of flow separation at the leading edge of the inboard pod juncture. While a lower Mach number ($M=0.75$) was chosen to minimize this effect, it can be seen that the pressure distribution predicted indicates that the Mach number before the shock wave is >1.5. This suggests that the flow might be separated despite the fact that the boundary layer scheme predicts no separation.

A second comparison set was generated using wing-body-nacelle data of Smith and Levin.[9] Correlations with experimental data can be found in Fig. 9. Recall that nacelle-off results for this condition were presented in Fig. 3. A dramatic interference effect induced by the nacelle is satisfactorily reproduced except for expansions apparent on the wing lower surface. This discrepancy might be caused by an inability to simulate a high pressure region aft of the nacelle base (Fig. 6b) which abruptly ends. Unlike the USB case, however, no flow separation is apparent.

Slipstream Modeling

Modeling the slipstream flow as a small perturbation to the undisturbed slipstream's ultimate wake, Eq. (1) is employed using

$$M_\infty = M_\infty(r) = \sqrt{5(1+0.2M_\infty^2)\left(\frac{P_T(r)}{P_{T_\infty}}\right)^{\frac{\gamma-1}{\gamma}} - 1} \tag{6}$$

Here $P_T(r)/P_{T_\infty}$ represents the ratio of total pressure in the slipstream to that in the freestream, and $M_\infty(r)$ is the Mach number in the slipstream ultimate wake (assuming isentropic flow so $P=P_\infty$). Pressure coefficients given by Eq. (2) are then corrected to freestream dynamic pressure

$$C_P = \frac{P-P_\infty}{q_\infty} = \frac{P-P_\infty}{q_\infty(r)}\frac{q_\infty(r)}{q_\infty}$$
$$= -[2\varphi_x + [1-M_\infty^2(r)]\varphi_x^2 + \varphi_y^2]\frac{M_\infty^2(r)}{M_\infty^2} \tag{7}$$

Finally, slipstream swirl velocities are superimposed on the otherwise irrotational flow. This requires a modification to the standard planar wing boundary condition

$$\varphi_z = (dz/dx) - \alpha \tag{8}$$

to give

$$\varphi_z = (dz/dx) - \alpha - W(r) \tag{9}$$

where $W(r)$ represents slipstream swirl.

Radial Mach distribution given by Eq. (6) is enforced by adjusting the Mach number for each spanwise plane along the wing which lies within the slipstream region. This represents a very coarse approximation since physical flow Mach variations are constrained to the cylindrical slipstream volume while computational Mach variations extend to vertical infinity above and below the wing using the present Cartesian scheme. While a cylindrical grid system would obviate the need for this approximation, correlations with experimental data indicate that there is no significant penalty associated with its use.

Total pressure and swirl data[8] for a slipstream simulator appear in Fig. 10. Computational distributions indicated in this figure were obtained by treating spanwise grid stations

Table 1 Effect of nacelles on force and moment coefficients

	Experiment	Present method
ΔC_L	−0.0560	−0.0310
ΔC_M	+0.0200	+0.0120
ΔC_D	−0.0004	−0.0021

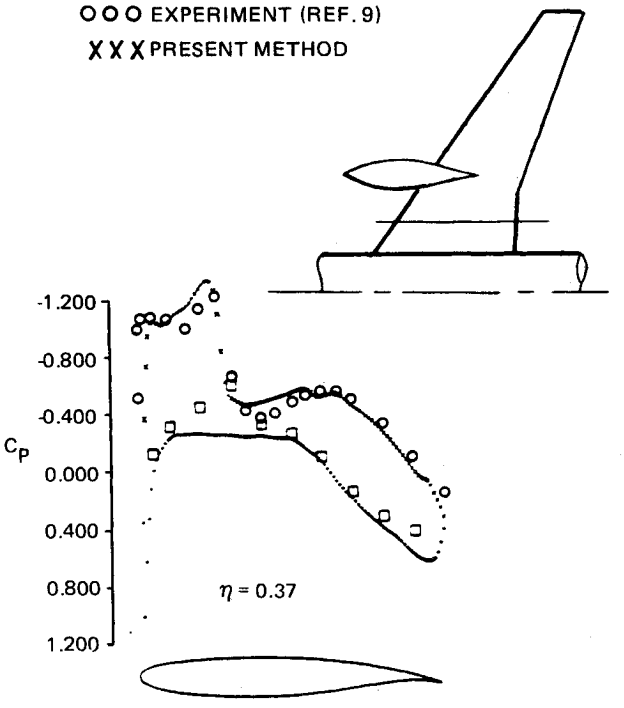

Fig. 9 Wing-body-nacelle pressure distribution correlation, $M=0.80$, $\alpha=1.83$ deg.

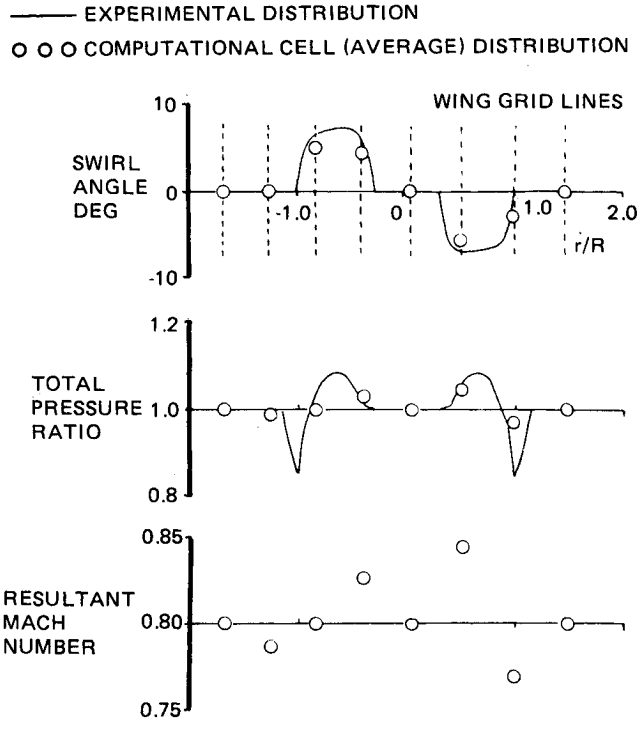

Fig. 10 Experimental/computational swirl, total pressure, and Mach number distributions.

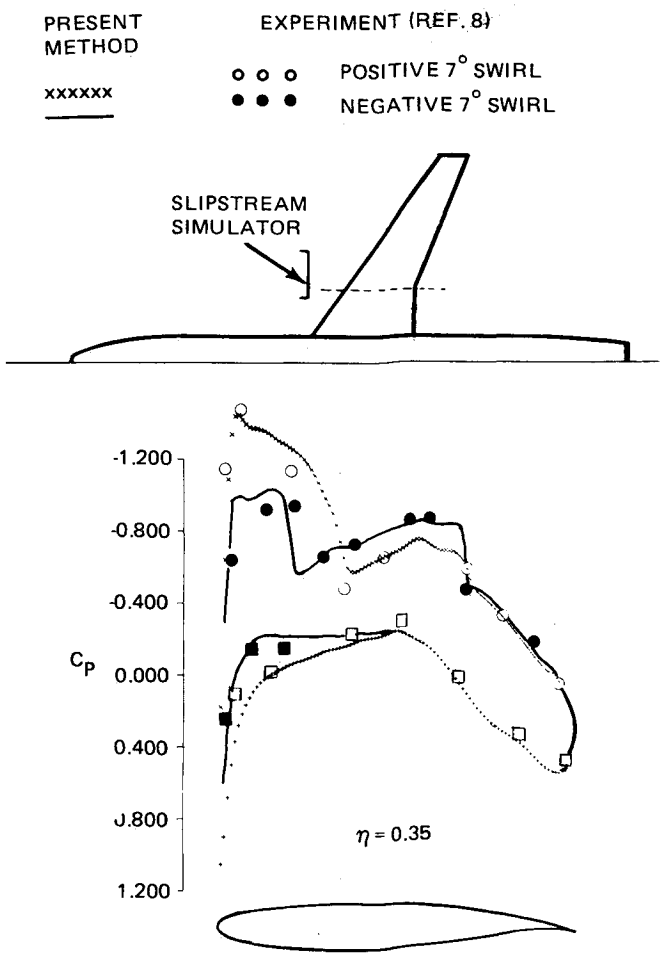

Fig. 11 Wing pressure distribution correlations for positive and negative swirl, $M=0.80$; $\alpha=3$ deg.

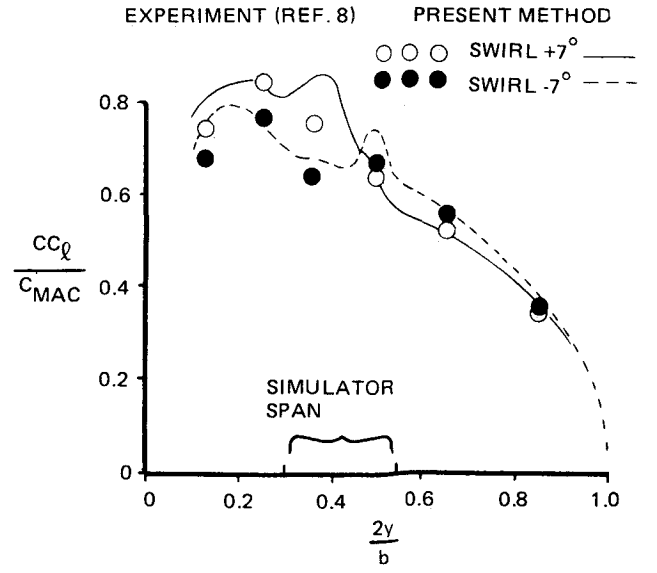

Fig. 12 Effect of swirl on wing spanload, $M=0.80$.

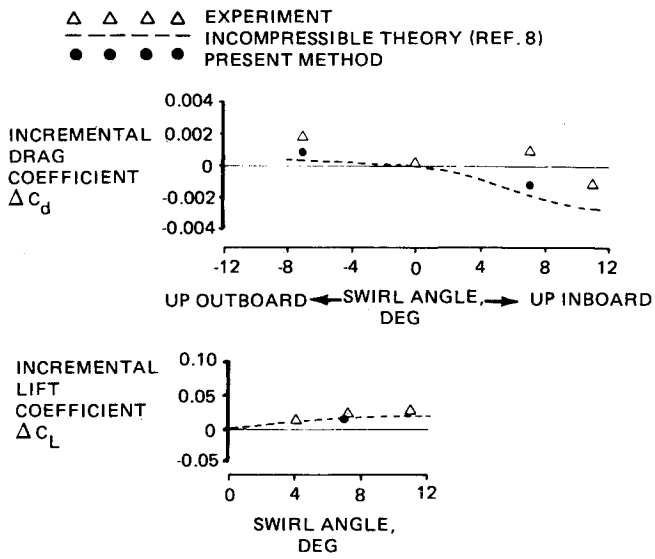

Fig. 13 Effect of slipstream swirl on configuration lift and drag, $M=0.80$.

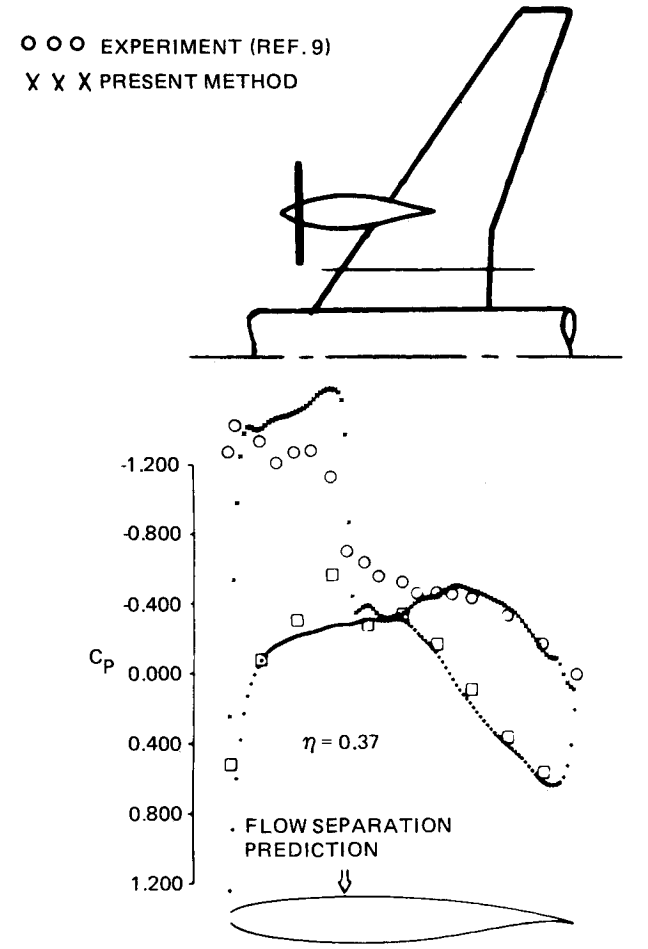

Fig. 14 Wing-body-nacelle slipstream pressure distribution correlation, $M=0.80$, $\alpha=1.83$ deg.

as cell centerlines and then using the average value across each cell width. This procedure provided a good flow simulation, though some smearing of slipstream properties probably occurs. For spanwise grid systems typically used in transonic finite difference codes (15-20 points), it is expected that this "averaging scheme" would minimize sensitivity of computed results to grid location. Figure 11 compares computed and experimental wing pressure distributions using this simple slipstream model at $M=0.80$ for ± 7 deg swirl. Recall that basic or clean wing pressure comparisons for this condition were included in Fig. 2. The effect of the two slipstreams on wing spanwise loading can be found in Fig. 12. The incremental lift and drag levels can be found in Fig. 13. Note that detailed pressure distributions agree quite well; but, surprisingly, drag and lift increments agree better with the incompressible theory[8] than with experimental data.

A similar set of comparisons was prepared using propeller-generated slipstream data.[9] These correlations are compromised somewhat by a separated flow region inboard of the nacelle (see Fig. 14). Unlike the USB-nacelle case (Fig. 8), however, the boundary layer method did predict that flow separation would occur at the inboard wing station. Note that comparisons without the slipstream were included in Fig. 9.

Conclusions

1) A transonic small-perturbation scheme appears to be quite satisfactory for prop-fan engine installation analyses. Current flow modeling capability is more constrained by the ability to satisfactorily predict and simulate separated flow regions (Figs. 8 and 14) than it is by the ability to simulate large disturbances induced by nacelles, slipstreams, and blunt supercritical airfoil sections (Figs. 9, 11). While the physical flow features unsteadiness and vorticity, it is not clear at this point in time what benefits will be obtained by explicitly modeling these flow elements.

2) Computational grid density and differencing scheme approximations appreciably affect shock wave resolution. For some applications, these factors will play a more important role in determining flow simulation quality than terms included in the flow governing equation.

3) A large portion of experimental data now used to validate computational schemes for prop-fan nacelle and slipstream models features separated flow. Comparisons which use these data require careful interpretation.

4) Flow separation has compromised an attempt to evaluate pressure and incremental force/moment prediction capability for both a simple nacelle (Table 1) and a propeller-generated slipstream (Fig. 14). For what appears to be attached flow, drag increments obtained using a slipstream simulator (Fig. 13) may be affected by simulator hardware upstream of the model.

5) Ref. 10 provides a more complete set of correlations.

References

[1]Boctor, M.L., Clay, C.W., and Watson, C.F., "An Analysis of Prop-fan/Airframe Aerodynamic Integration," NASA CR-152186, 1978.

[2]Rizk, M.H., "Aerodynamic Effects of Nearly Uniform Slipstreams on Thin Wings in the Transonic Regime," NASA CR-152351, 1980.

[3]Welge, H.R., Neuhart, D.H., and Dahlin, J.A., "Analysis of Mach Number 0.8 Turboprop Slipstream Wing/Nacelle Interactions," NASA CR-166214, 1981.

[4]Whitfield, D.L. and Jameson, A., "Three-Dimensional Euler Equation Simulation of Propeller-Wing Interaction in Transonic Flow," AIAA Paper 83-0236, Jan. 1983.

[5]Narain, J.P., "A Transonic Analysis of Propfan Slipstream Effect on a Supercritical Wing," AIAA Paper 83-0186, Jan. 1983.

[6]Samant, S.S., Yu, N.J., and Rubbert, P.E., "Transonic Flow Simulation of Propfan Configurations," AIAA Paper 83-0187, Jan. 1983.

[7]Boppe, C.W., "Transonic Flow Analysis for Wing-Fuselage Configurations," NASA CR-3243, 1980.

[8]Welge, H.R. and Crowder, J.P., "Simulated Propeller Slipstream Effects on a Supercritical Wing," NASA CR-152138, 1978.

[9]Smith, R.C. and Levin, A.D., "Propfan Installation Aerodynamics of a Supercritical Swept Wing Transport Configuration," AIAA Paper 81-1563, July 1981.

[10]Boppe, C.W. and Rosen, B.S., "Computation of Prop-Fan Engine Installation Aerodynamics," ICAS 84-5.5.3, Sept. 1984.